Received: 8 October 2022 | Accepted: 21 December 2022

DOI: 10.1002/pamm.202200213

Patient-specific simulation of brain tumour growth and regression

Marlon Suditsch[1,2,3,*], **Tim Ricken**[2,3], and **Arndt Wagner**[1,3]

[1] Institute of Applied Mechanics (CE), University of Stuttgart, 70569 Stuttgart, Germany
[2] Institute of Structural Mechanics and Dynamics in Aerospace Engineering, University of Stuttgart, 70569 Stuttgart, Germany
[3] Stuttgart Center for Simulation Science (SC SimTech), University of Stuttgart, 70569 Stuttgart, Germany

The medical relevance of brain tumours is characterised by its locally invasive and destructive growth. With a high mortality rate combined with a short remaining life expectancy, brain tumours are identified as highly malignant. A continuum-mechanical model for the description of the governing processes of growth and regression is derived in the framework of the Theory of Porous Media (TPM). The model is based on medical multi-modal magnetic resonance imaging (MRI) scans, which represent the gold standard in diagnosis. The multi-phase model is described mathematically via strongly coupled partial differential equations. This set of governing equations is transformed into their weak formulation and is solved with the software package FEniCS. A proof-of-concept simulation based on one patient geometry and tumour pathology shows the relevant processes of tumour growth and the results are discussed.

1 Introduction

A tumour disease is characterised by abnormal or uncontrolled cell proliferation, that is out of sync with the organism's requirements for normal tissue, cf. [1]. Specifically, glioblastomas are malignant astrocytic tumours, representing the most common brain tumours in adults. The medical relevance of brain tumours is mainly reflected by a high mortality and a low remaining life expectancy. In addition, histologically benign tumours can also lead to an increased mortality rate, cf. [2]. From [3], respectively the publicly accessible database query [4], the case numbers of incidence and mortality of different types of cancer are compared in Table 1. It becomes obvious that even though cancers of the central nervous system occur less frequently than other cancers, they typically lead to death more rapidly. The median age of onset of the disease for women is 65 years (63 years men) and the median age of death for women is 69 years (67 years men). The cause of brain tumours is still largely unknown, while the risk of contracting the disease is slightly increased in the case of radiation therapy. Genetic inheritance is known for increasing the relative risk of a disease. A correlation between mobile phone use and brain tumours is being discussed, as well as exposure to pesticides from agriculture.

	Incidences		**Mortality**	
Category	Female	Male	Female	Male
C00 - C96 (without C44)	234 514	265 396	104 791	124 274
C70 - C72	3162	4112	2615	3441
C71	2974	3930	2575	3406

Table 1: Case numbers of incidence and mortality in Germany (2018). Split by gender for cancer diseases in total (C00 - C96), in the central nervous system (C70 - C72) and particulary in the brain (C71). Data collected by [4].

For a non-invasive diagnosis, the widely used magnetic resonance imaging (MRI) has been established. MRI can be used with different modalities by the well-trained clinician. A possible treatment of brain tumour diseases mainly consists of three different approaches, while in the case of a malignant tumour, surgical removal is preferred. However, since the brain is responsible for many important tasks, cutting out areas with a large margin is not common. Therefore, an attempt to prevent the tumour from spreading can consist in radiation or injecting, respectively implanting, a chemotherapeutic agent.
According to [5], the foundations of neurosurgery consist primarily on a well-planned surgical strategy based on the anatomical knowledge and the understanding of the information provided by imaging. Tumour segmentation is a supportive visualising tool in diagnosis that helps by emphasizing the distribution of the tumour compartments. On top of that, a well-designed model that is capable of describing the relevant processes can be of immense benefit.

2 Image-based diagnosis procedures and processing

With image-based approaches, typically two-dimensional image series along different axes are produced, that can be assembled into three-dimensional objects and viewed by using tools such as freeview from freesurfer [6]. The general geometry of

* Corresponding author: e-mail marlon.suditsch@mechbau.uni-stuttgart.de, phone +49 711 685 66343

the brain, but also possible tumours, can be determined using structural MRI scans. The BRaTS challenge [7] set the gold standard for multi-modal image recognition on four different modalities. Herein, scans with two different relaxation times T1 and T2, as well as a fluid-attenuated inversion recovery scan (FLAIR) and scans with contrast agent gandolium (T1Gd), which visualises the separation of free to bound fluid, are included, see Figure 1.

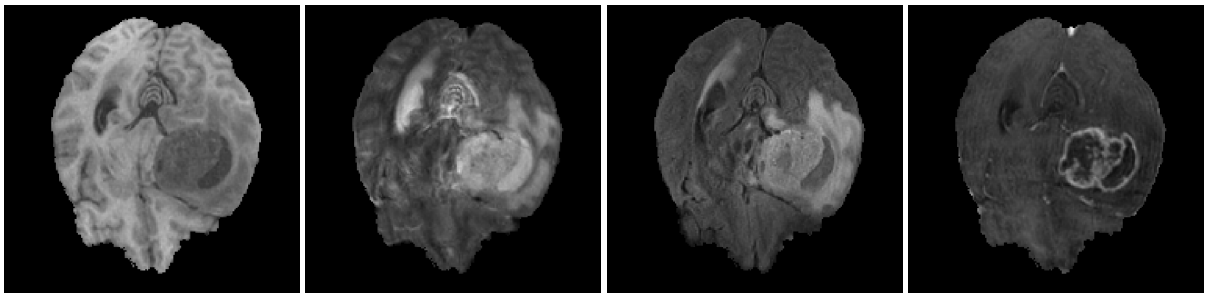

Fig. 1: Four different structural MRI modalities from left to right: T1-weighted relaxation time, T2-weighted relaxation time, fluid-attenuated inversion recovery (FLAIR) scan and T1Gd-weighted scan with contrast agent gandolium.

Since 2012, submissions from participants of the BraTS challenge [7, 8] reflect the developments in digital imaging of multi-modal tumour segmentation. With the help of artificial neural networks, it is thus possible to automatically localise and identify the tumour with its sub-regions via MRI scans. Since 2017, the tumour sub-regions considered for evaluation are: 1) the active solid tumour, 2) the necrotic (fluid-filled) and the non-enhancing (solid) parts of the tumour and 3) the peritumoral edematous/invaded tissue, see Figure 2. In 2020, a prediction of the remaining lifetime of the subject in days was brought into being. The results show the difficulties of previously known machine learning methods when the available data set is very small. Although a simple numerical value about the prognosis of the remaining lifetime is an important and meaningful indicator, it does not provide any information about the further behaviour of the tumour with or without a specific treatment method. It also does not provide any information about the course of the disease. In the following, a data-driven continuum-mechanical model is presented, which provides a possible spatial tumour evolution with the filtered information from a pre-processing of the multi-modal MRI scans.

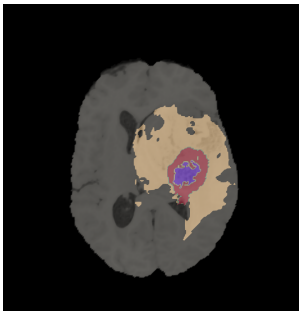

Fig. 2: Tumor segmentation [7], necrotic core and inactive solid tumour in blue, active tumour in red and edematous tissue in orange.

3 Continuum-mechanical modelling approach

Referring to [9–11], the continuum-mechanical perspective of the problem is formulated in the framework of the Theory of Porous Media (TPM). Herein, the brain's microstructure is divided into separable continua and homogenised over a representative volume element $\mathrm{d}v$. In particular, it is separated into constituents for the solid φ^S and the interstitial fluid φ^I, where φ^S splits into healthy cells with the skeleton of the extracellular matrix (ECM) φ^{Sh} and the solidificated tumour φ^{St}. The fluid constituent can be divided into a solute phase φ^{Is}, wherein nutrients φ^{In} in form of glucose, mobile tumour cells φ^{It} and vascular endothelial growth factors (VEGF) φ^{Iv} are solved, viz.:

$$\varphi = \bigcup_{\alpha} \varphi^{\alpha} = \varphi^S \cup \varphi^I = \left(\varphi^{Sh} \cup \varphi^{St}\right) \cup \left(\varphi^{Is} \cup \varphi^{In} \cup \varphi^{It} \cup \varphi^{Iv}\right) . \tag{1}$$

By defining the scalar structure variable, the volume fraction

$$n^{\alpha} := \frac{\mathrm{d}v^{\alpha}}{\mathrm{d}v} \qquad \text{with} \quad \mathrm{d}v = \sum_{\alpha} \mathrm{d}v^{\alpha} , \tag{2}$$

the local composition of immiscible constituents φ^{α} (with $\alpha = \{S, I\}$) can be quantified with its particular partial volume $\mathrm{d}v^{\alpha}$. In that way, the saturation of each material point is given by

$$\sum_{\alpha} n^{\alpha} = 1 , \tag{3}$$

which results in a natural constraining condition. The fluid is composed of miscible components $\varphi^{I\gamma}$ with $\gamma = \{s, n, t, v\}$. They can be measured analogous with the definitions of the molar concentration $c_m^{I\gamma}$ of a component $\varphi^{I\gamma}$, its constant molar mass $M_m^{I\gamma}$ and the respectve partial density $\rho^{I\gamma}$, with

$$c_m^{I\gamma} := \frac{\mathrm{d}n_m^{I\gamma}}{\mathrm{d}v^I} \qquad \text{and} \qquad M_m^{I\gamma} := \frac{\mathrm{d}m^{I\gamma}}{\mathrm{d}n_m^{I\gamma}} \qquad \text{and} \qquad \rho^{I\gamma} := n^I \rho_I^{I\gamma} . \tag{4}$$

Herein, the relations of the number of moles $\mathrm{d}n_m^{I\gamma}$ to the bulk fluid volume $\mathrm{d}v^I$ and the mass $\mathrm{d}m^{I\gamma}$ of a component are used. The partial density $\rho^{I\gamma}$ is related to the partial pore density $\rho_I^{I\gamma}$ via the already introduced volume fraction n^I. With that, the partial density of the fluid ρ^I and its effective density $\rho^{I\mathrm{R}}$ can be formulated with

$$\rho^I = \sum_\gamma \rho^{I\gamma} \qquad \text{and} \qquad \rho^{I\mathrm{R}} = \sum_\gamma \rho_I^{I\gamma}\,, \qquad \text{with} \qquad \rho_I^{I\gamma} = c_m^{I\gamma} M_m^{I\gamma}\,. \tag{5}$$

Material incompressible constituents and components are assumed with $\rho^{\alpha\gamma\mathrm{R}} = \mathrm{const.}$ and vanishingly small volume fractions of solved components in the fluid in comparison to its base liquid with

$$n^{Is} \gg \{n^{In}, , n^{It}, n^{Iv}\} \qquad \text{leads to} \qquad \rho^{Is\mathrm{R}} \approx \rho^{I\mathrm{R}} \qquad \text{and} \qquad n^{Is} \approx n^I\,. \tag{6}$$

Furthermore, the partial velocity $\overset{\prime}{\mathbf{x}}_{I\gamma}$, the seepage velocity $\mathbf{w}_{I\gamma} = \overset{\prime}{\mathbf{x}}_{I\gamma} - \overset{\prime}{\mathbf{x}}_S$ and the diffusive velocity $\mathbf{d}_{I\gamma} = \overset{\prime}{\mathbf{x}}_{I\gamma} - \overset{\prime}{\mathbf{x}}_I$ of a component $\varphi^{I\gamma}$, for φ^{Is} in particular, is simplified to

$$\overset{\prime}{\mathbf{x}}_{Is} \approx \overset{\prime}{\mathbf{x}}_I\,, \quad \mathbf{w}_{Is} \approx \mathbf{w}_I \quad \text{and} \quad \mathbf{d}_{Is} = \mathbf{0}\,. \tag{7}$$

φ^{St} and φ^{Sh} are somehow connected tissues, which is why a common movement function is assumed. Thus, the velocities of the solid components become

$$\overset{\prime}{\mathbf{x}}_{St} \;\equiv\; \overset{\prime}{\mathbf{x}}_{Sh} \;\equiv\; \overset{\prime}{\mathbf{x}}_S\;. \tag{8}$$

Since the phenomena are considered with no pronounced temperature changes ($\Theta^\alpha = \Theta = \mathrm{const.}$), the consideration of the balance of energy of a constituent or component can be omitted. The quasi-static processes of tumour growth can be expressed via neglection of the acceleration and the quadratic velocities of the aggregate and the constituents, respectively

$$\ddot{\mathbf{x}} \;\equiv\; \overset{\prime\prime}{\mathbf{x}}_\alpha \;\equiv\; \mathbf{0} \qquad \text{and} \qquad \overset{\prime}{\mathbf{x}}_\alpha \cdot \overset{\prime}{\mathbf{x}}_\alpha = 0\,. \tag{9}$$

Since angular momentum productions are assumed to be zero ($\hat{\mathbf{m}}^\alpha = \mathbf{0}$), the evaluation of the angular momentum equations leads to symmetric partial Cauchy stresses $\mathbf{T}^\alpha = (\mathbf{T}^\alpha)^{\mathrm{T}}$. The observation of a floating brain in its skull justifies the assumption of neglecting body forces $\mathbf{b}^\alpha = \mathbf{b} = \mathbf{0}$ and the governing equations are finally derived, taking into consideration Truesdell's metaphysical principles [12], via a combination of the balance of mass and linear momentum of each constituent, viz.:

$$0 = (\rho^\alpha)'_\alpha + \rho^\alpha \operatorname{div} \overset{\prime}{\mathbf{x}}_\alpha - \hat{\rho}^\alpha \qquad \text{and} \qquad \mathbf{0} = \operatorname{div} \mathbf{T}^\alpha + \hat{\mathbf{p}}^\alpha\,. \tag{10}$$

The governing equations pose a set of coupled partial differential equations (PDE). The first PDE derives by adding up the momentum equations of each constituent in Equation $(11)_1$. A second PDE, the volume balance of the fluid constituent, which is expressed with relative displacement of the solid body in Equation $(11)_2$, is evaluated with the relation $\rho^\alpha = n^\alpha \rho^{\alpha\mathrm{R}}$ and the assumption of incompressible constituent. Finally, the molar concentration balances of the solved components in the liquid solvent in Equation $(11)_3$ correspond to the mass balances referred to the solid displacement, viz.:

$$\begin{aligned}
\mathbf{0} = &\quad \operatorname{div} \mathbf{T} + \hat{\mathbf{p}} \qquad \text{with} \qquad \sum_\alpha \left(\hat{\mathbf{p}}^\alpha + \hat{\rho}^\alpha \overset{\prime}{\mathbf{x}}_\alpha \right) = \mathbf{0}\,, \\
0 = &\quad (n^I)'_S + \operatorname{div}(n^I \mathbf{w}_I) + n^I \operatorname{div} \overset{\prime}{\mathbf{x}}_S - \frac{\hat{\rho}^I}{\rho^{I\mathrm{R}}}\,, \\
0 = &\quad n^I (c_m^{I\gamma})'_S + \operatorname{div}(n^I c_m^{I\gamma} \mathbf{w}_{I\gamma}) + c_m^{I\gamma} \left(\operatorname{div} \overset{\prime}{\mathbf{x}}_S - \frac{\hat{\rho}^S}{\rho^S} \right) - \frac{\hat{\rho}^{I\gamma}}{M_m^{I\gamma}}\,.
\end{aligned} \tag{11}$$

According to Coleman and Noll [13], the problem is closed in a thermodynamically consistent modelling process. Herein, proportionality relations can be found. In this regard, a Darcy-like equation for the seepage velocity

$$n^I \mathbf{w}_I = -\frac{\mathbf{K}^I}{\gamma^{IR}} \operatorname{grad} p\,, \tag{12}$$

with the hydraulic (Darcy) permeability tensor $\mathbf{K}^I$, the effective fluid weight γ^{IR} and the overall pore pressure $p^{I\mathrm{R}}$, is obtained. Analogously, a Fickean diffusion velocity for the solved components in the carrier fluid, with a particular diffusion parameter $\mathbf{D}^{I\gamma}$, can be derived to

$$n^I c_m^{I\gamma} \mathbf{w}_{I\gamma} = -\mathbf{D}^{I\gamma} \operatorname{grad} c_m^{I\gamma} + n^I c_m^{I\gamma} \mathbf{w}_I\,. \tag{13}$$

The isotropic part of the finite Neo-Hookean solid extra stress is choosen, viz.:

$$\mathbf{T}_{\mathrm{E}}^S = 2\frac{\mu^S}{\mathrm{J}_S} \mathbf{E}_S + \lambda^S (1 - n_{0S}^S)^2 \left(\frac{1}{1 - n_{0S}^S} - \frac{1}{\mathrm{J}_S - n_{0S}^S} \right) \mathbf{I}\,, \tag{14}$$

Herein, λ^S and μ^S are the Lamé parameters, J_S is the Jacobian, n^S_{0S} is the initial volume fraction and $\mathbf{E}_S$ is the Green-Lagrangean strain measure of the solid body. Furthermore, $\mathbf{I}$ is the identity tensor. The individual volume fractions of the solid constituent $\varphi^{S\delta}$ with $\delta = \{h, t\}$ are resolved implicitly via their volume balances by

$$n^{S\delta} = n^{S\delta}_g \mathrm{J}_S^{-1} \qquad \text{and} \qquad n^{S\delta}_g = n^{S\delta}_0 \exp\left(\int_{t_0}^{t} \frac{\hat{n}^{S\delta}}{n^{S\delta}} \mathrm{d}\tilde{t}\right) . \tag{15}$$

Herein, $\hat{n}^{S\delta}$ is the volume production. By considering the relevant proccesses for tumour growth and regression, cf. [14], the mass-production terms build the essential driving forces in this model, viz.:

$$\sum_{\alpha} \hat{\rho}^{\alpha} = 0 \quad \text{with} \quad \hat{\rho}^S = \hat{\rho}^{St} = \hat{\rho}^{St}_{\oplus} + \hat{\rho}^{St}_{\ominus} \quad \text{and} \quad \hat{\rho}^I = \sum_{\gamma} \hat{\rho}^{I\gamma} \quad \text{with} \quad \hat{\rho}^{I\gamma} = \hat{\rho}^{I\gamma}_{\oplus} + \hat{\rho}^{I\gamma}_{\ominus} . \tag{16}$$

Herein, Equation $(16)_1$ ensures a closed-system approach and Equation $(16)_2$ shows the general split into gains and losses. The production term of the constituent sums up the production terms of the respective components, see Equation $(16)_3$. The production term of the healthy cells is assumed to be zero, since the organism tries to be in homeostasis. For a more comprehensive and detailed discussion, reference is made to [15], where the proliferation production terms follow a Monod kinetic and the processes of metabolism and angiogenesis remain linear. In the following, a linear relation for necrosis is also assumed.

4 Numerical investigations

In building up a test case with a real geometry and tumour pathology, subject 57 from the BraTS 2020 dataset[1] is selected as an example and provides MRI scans and a manually corrected tumour segmentation. In order to generate an initial boundary value problem, the three-dimensional NifTi[2] image data must be processed. Inspired by [16], a watertight surface mesh is generated from the solid brain geometry by using NII2MESH[3] and the resulting file is converted into a finite volume mesh using SVMTK[4] (.mesh file). Finally, it can be converted into the desired file format (.xdmf) with MESHIO[5], see Figure 3.

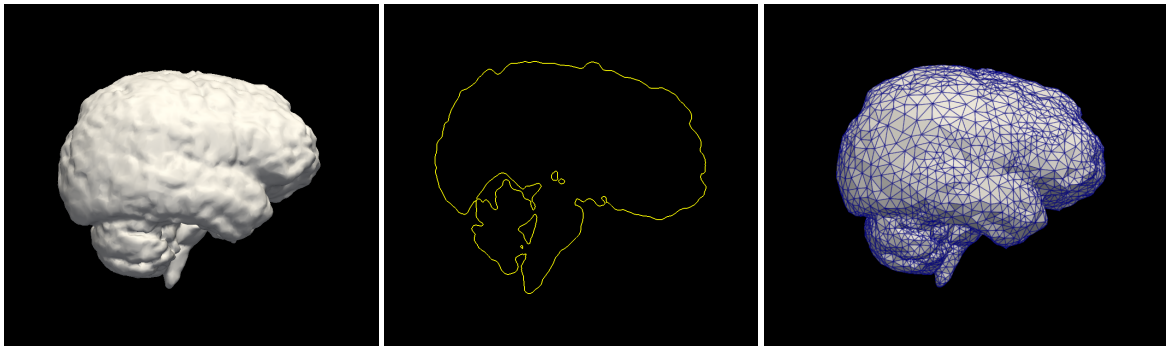

Fig. 3: Workflow of patient-specific data (subject 57, BraTS 2020) from NifTi 3D image (left) over watertight surface mesh (center) to processable volume mesh (right).

The tumour segmentation is projected onto the resulting geometry, see Figure 4. To generate a more realistic initial distribution of the tumour compartments, the respective quantity is set to its maximal value ($n^{St,\max}$, $c_m^{It,\max}$) in their respective centre. Setting $c_m^{It,\max}$ generally in the domain of n^{St}. From here, a linear interpolation is made to a minimal value at their outer edge, see Figure 5. For the numerical implementation of the initial boundary value problem, the software toolbox FEniCS[6] is selected and the problem is solved with the well-known Finite Element Method. Therefore, the set of governing equations is backmapped

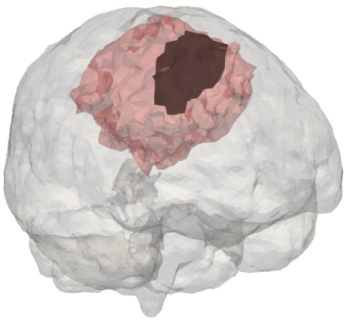

Fig. 4: Tumour mapping on preserved geometry. c_m^{It} in red, n^{St} in black.

[1] https://www.med.upenn.edu/cbica/brats2020/data.html
[2] https://nifti.nimh.nih.gov/
[3] https://github.com/neurolabusc/nii2mesh
[4] https://github.com/SVMTK/SVMTK
[5] https://github.com/nschloe/meshio
[6] https://fenicsproject.org/

to the reference configuration and formulated into their weak forms, viz.:

$$
\begin{aligned}
\mathcal{G}_{\mathbf{u}_S}: \quad & \int_{\Omega_0} \mathbf{P} \cdot \operatorname{Grad} \delta\mathbf{u}_S \,\mathrm{d}V - \int_{\Omega_0} \mathrm{J}_S \frac{\hat{\rho}^S}{n^I} \frac{\mathbf{K}^I}{\gamma^{I\mathrm{R}}} \operatorname{Grad} p^{I\mathrm{R}} \,\mathbf{F}_S^{-1} \delta\mathbf{u}_S \,\mathrm{d}V - \int_{\partial\Omega_0} \mathbf{P} \cdot \mathbf{N} \,\delta\mathbf{u}_S \,\mathrm{d}A = 0\,, \\
\mathcal{G}_{p^{I\mathrm{R}}}: \quad & \int_{\Omega_0} \mathrm{J}_S \left[(n^I)'_S - \frac{\hat{\rho}^I}{\rho^{I\mathrm{R}}} \right] \delta p^{I\mathrm{R}} \,\mathrm{d}V + \int_{\Omega_0} \mathrm{J}_S \, n^I \, \mathbf{D}_S \cdot \mathbf{I} \,\delta p^{I\mathrm{R}} \,\mathrm{d}V + \\
& + \int_{\Omega_0} \mathrm{J}_S \frac{\mathbf{K}^I}{\gamma^{I\mathrm{R}}} \operatorname{Grad} p^{I\mathrm{R}} \,\mathbf{C}_S^{-1} \cdot \operatorname{Grad} \delta p^{I\mathrm{R}} \,\mathrm{d}V - \int_{\partial\Omega_0} \mathrm{J}_S \frac{\mathbf{K}^I}{\gamma^{I\mathrm{R}}} \operatorname{Grad} p^{I\mathrm{R}} \,\mathbf{C}_S^{-1} \cdot \mathbf{N} \,\delta p^{I\mathrm{R}} \,\mathrm{d}A = 0\,, \\
\mathcal{G}_{c_m^{I\gamma}}: \quad & \int_{\Omega_0} \mathrm{J}_S \left[n^I (c_m^{I\gamma})'_S - c_m^{I\gamma} \frac{\hat{\rho}^S}{\rho^S} - \frac{\hat{\rho}^{I\gamma}}{M_m^{I\gamma}} \right] \delta c_m^{I\gamma} \,\mathrm{d}V + \int_{\Omega_0} \mathrm{J}_S \, c_m^{I\gamma} \, \mathbf{D}_S \cdot \mathbf{I} \,\delta c_m^{I\gamma} \,\mathrm{d}V + \\
& + \int_{\Omega_0} \mathrm{J}_S \left(\mathbf{D}^{I\gamma} \operatorname{Grad} c_m^{I\gamma} + c_m^{I\gamma} \frac{\mathbf{K}^I}{\gamma^{I\mathrm{R}}} \operatorname{Grad} p^{I\mathrm{R}} \right) \mathbf{C}_S^{-1} \cdot \operatorname{Grad} \delta c_m^{I\gamma} \,\mathrm{d}V - \\
& - \int_{\partial\Omega_0} \mathrm{J}_S \left(\mathbf{D}^{I\gamma} \operatorname{Grad} c_m^{I\gamma} + c_m^{I\gamma} \frac{\mathbf{K}^I}{\gamma^{I\mathrm{R}}} \operatorname{Grad} p^{I\mathrm{R}} \right) \mathbf{C}_S^{-1} \cdot \mathbf{N} \,\delta c_m^{I\gamma} \,\mathrm{d}A = 0\,,
\end{aligned}
\tag{17}
$$

with the expressions of the Piola-Kirchhoff stress $\mathbf{P} = \mathrm{J}_S \mathbf{T} \mathbf{F}_S^{-\mathrm{T}}$, the symmetric deformation velocity $\mathbf{D}_S = \frac{1}{2}(\mathbf{L}_S + \mathbf{L}_S^{\mathrm{T}})$, the material velocity gradient $\mathbf{L}_S = (\mathbf{F}_S)'_S \mathbf{F}_S^{-1}$, the right Cauchy-Green tensor $\mathbf{C}_S = \mathbf{F}_S^{\mathrm{T}} \mathbf{F}_S$, the deformation gradient $\mathbf{F}_S := \frac{\partial \mathbf{x}}{\partial \mathbf{X}_S}$, with its definition in mapping the actual position $\mathbf{x}$ to the reference position $\mathbf{X}_S$ of a material point with respect to the solid, the outward directed normal $\mathbf{N}$ and the solid constituents $\delta = \{h, t\}$, respective fluid components $\gamma = \{n, t, v\}$. The set of primary variables $\{\mathbf{u}_S, p^{I\mathrm{R}}, c_m^{I\gamma}\}$ is discretised in space by a Taylor-Hood element formulation, with second order ansatz functions for the displacements $\mathbf{u}_S$ and linear ansatz functions for the remaining degrees of freedom. In time, it is discretised with the time-step independent implicit Euler scheme of first order. The resulting mesh in this case contains over 151 000 tetrahedral elements connected by about 29 000 nodes. This results in over 200 000 degrees of freedom that must be calculated at each time step. The calculation time for each time step is less than 140 seconds on a single Intel Core i7-9700K with 126 GB memory at 3.60 clock speed. The three-dimensional structure is fixed in each spatial direction on the surface of the brainstem at the bottom of the brain ($\mathbf{u}_S = \mathbf{0}$ at $\partial\Omega_0$). According to [17], the intracranial pressure is assumed to be $p^{I\mathrm{R}} = 1466.5\,\mathrm{N/m^2}$. Referring to [15], the nutrient supply is assumed to be a constant Dirichlet concentration of $c_m^{In} = 1\,\mathrm{mol/m^3}$ over the total surface area. Figure 6 shows the initial state and the calculation result after the final calculation step of one month (30 days). The initial volume fraction of the solid tumour $\bar{n}^{St}$ is estimated from the grayscale of the MRI scan and the growth parameters are chosen according to [15] and references therein. However, no drug infusion is considered in this contribution. The mobile cancer cells continue to spread in the domain and its molar concentration c_m^{It} increases. The solid tumour body also grows slightly spatially and gains mass via an increasing volume fraction n^{St}. Angiogenesis is already in progress in tumours of this size and the tumour is supplied via a developed vascular system for increased nutrient delivery. Nevertheless, it can be seen in Figure 6, bottom left, that the supply is not completely sufficient and that there is a nutrient undersupply in the centre of the tumour, which causes necrosis.

5 Conclusion

The previously discussed model from [18, 19] is applied in this contribution to a real-case geometry with a valid tumour segmentation from clinical MRI data, with the calculation showing the expected behaviour. The model reflects all important process sequences. Possible improvements in modelling brain tumours, such as glioblastomas, at the organ scale could be achieved by further adjustments. In order to simplify the model, the concentration of VEGF could be omitted since the tumour must already have been vascularised for growing beyond a circumference of 1-2 mm, cf. [20]. With an additional tumour phase for the necrotic tumour part, the model can be adapted even more precisely to the medical data basis of the MRI scans and more accurate results can be expected. For the investigation of larger studies, unlike the constantly growing BraTS dataset, an automated environment is needed. Also, for older datasets or datasets with longitudinal measurement series, it is necessary to be able to create tumour segmentations that automatically generate valid results.

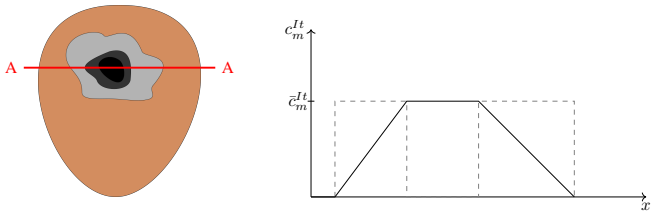

Fig. 5: Left: Cross-sectional view of tumour segmentation. Right: Tumour distribution mapping over A-A. The initial tumour edema distribution (gray, dashed) from the tumour segmentation is mapped into a partwise linear-constant distribution for the mobile cancer cells.

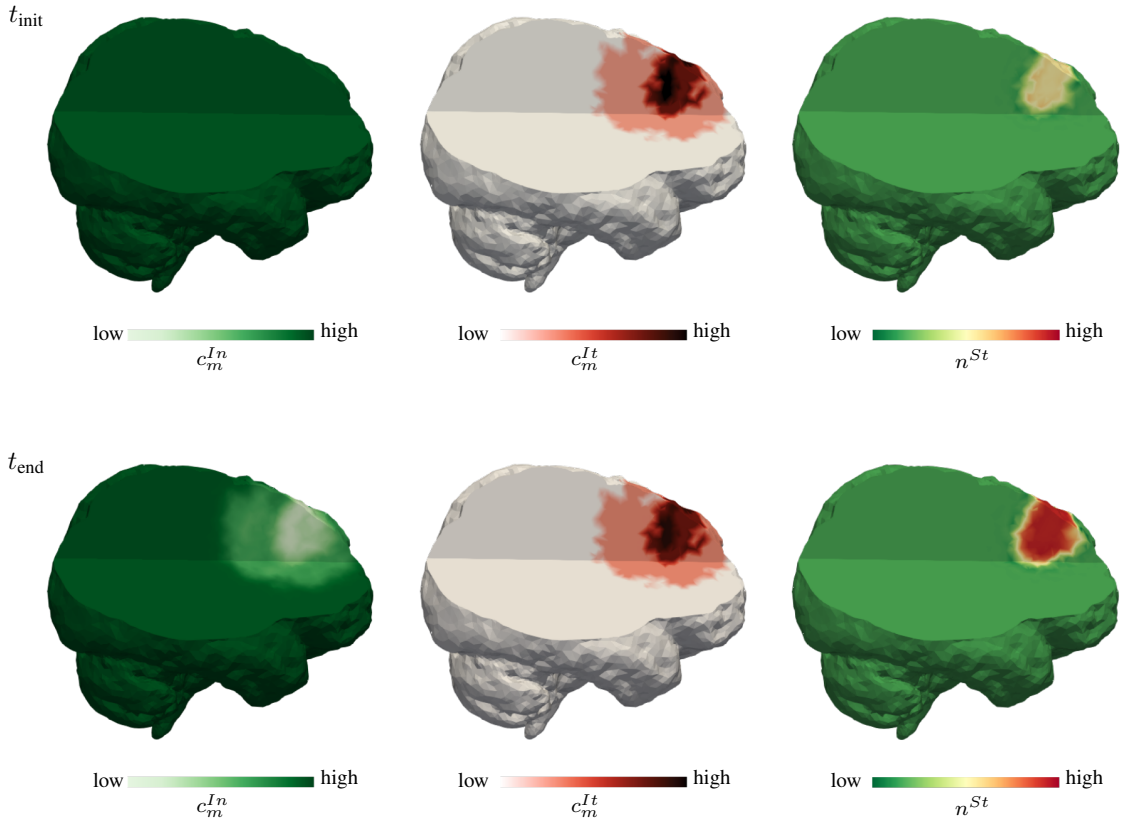

Fig. 6: Left: nutrient concentration c_m^{In}, Center: mobile cancer cell concentration c_m^{It}, Right: volume fraction solid tumour n^{St}, from initial time step (top row) to final time step (bottom row). The Patient-specific data is taken from [7].

In addition to structural MRI scans, related techniques such as diffusion tensor imaging (DTI) or dynamic susceptibility contrast (DSC) are emerging. Taking these modalities into account, fibre directions could be used to determine the spread of the tumour, or perfusion data could be included to determine the spatial nutrient supply. In order to make use of that information, particular parts of the model need to be reformulated, for example the implementation of a fiber-dependent Darcy flow. However, an inclusion of additional data will further improve the accuracy of the model and will hopefully help in supporting surgical intervention or chemotherapeutic treatment in the future.

Acknowledgements Funded by Deutsche Forschungsgemeinschaft (DFG, German Research Foundation) under Germany's Excellence Strategy EXC 2075 390740016. Open access funding enabled and organized by Projekt DEAL.

References

[1] World Health Organization (WHO), International Classification of Diseases, Eleventh Revision (ICD-11), 2019/2021
[2] K. Kraywinkel, C. Spix, Der Onkologe **25**, (2018)
[3] F. Erdmann et al., Krebs in Deutschland für 2017/2018, (Robert-Koch-Institut, Berlin, 2021)
[4] Z. f. Krebsregisterdaten (ZfKD), Datensatz des ZfKD auf Basis der epidemiologischen Landeskrebsregisterdaten, (ZfKD, Berlin, 2022)
[5] H. R. Winn, Youmans and Winn Neurological Surgery 4 - Volume Set, (Elsevier, Amsterdamm, 2022)
[6] B. Fischl, Neuroimage **62(2)**, 774-781 (2012)
[7] S. Bakas et al., arXiv, https://doi.org/10.48550/arXiv.1811.02629 (2018)
[8] B. H. Menze, IEEE Transactions on Medical Imaging **34**, 1993–2024 (2015)
[9] R. de Boer, Theory of Porous Media (Springer, Berlin, 2000)
[10] W. Ehlers, Porous media: theory, experiments and numerical applications (Springer, Berlin, 2002)
[11] A. Wagner, Continuum mechanics of multicomponent materials, habilitation, University of Stuttgart, 2021
[12] C. Truesdell, Rational Thermodynamics (Springer, New York, 1984)
[13] B. D. Coleman, W. Noll, Archive for Rational Mechanics and Analysis **13**, 167 - 178 (1963)
[14] D. Hanahan, R. A. Weinberg, Cell **100**, 2000
[15] W. Ehlers et al., Biomech Model Mechanobiol **21**, 277-315 (2022)
[16] K. -A. Mardal, Mathematical modeling of the human brain (Springer, 2022)

[17] M. J. Albeck et al., J Neurosurg **74**, 597–600 (1991)
[18] M. Suditsch et al., PAMM **20**, (Wiley, 2021)
[19] M. Suditsch et al., PAMM **21**, (Wiley, 2022)
[20] I. Bačić, et al., Oncol Lett **15**, 2335-2339 (2018)